

PREDICTION OF THE CUTTING TEMPERATURES OF TURNING STAINLESS STEEL WITH CHAMFERED CUTTING EDGE NOSE RADIUS TOOLS

CHUNG-SHIN CHANG

Department of Mechanical and Electro-Mechanical Engineering
National Ilan University
No. 1, Shen-Lung Road
I-Lan City, 260
Taiwan, R.O.C.
e-mail: cschang@ydu.edu.tw
cschang@niu.edu.tw

Abstract

Temperatures of the carbide tip's surface, when turning stainless steel with a chamfered main cutting edge nose radius tool are investigated. The mounting of the carbide tip in the tool holder is ground to a nose radius as measured by a toolmaker microscope, and a new cutting temperature model developed from the variations in shear and friction plane areas occurring in tool nose situations are presented in this paper. The frictional forces and heat generated in the basic cutting tools are calculated by using the measured cutting forces and the theoretical cutting analysis. The heat partition factor between the tip and chip is solved by the inverse heat transfer analysis, which utilizes the temperature on the *P*-type carbide tip's surface measured by infrared as the input. The tip's carbide surface temperature is determined by finite element analysis (FEA), and compared with temperatures obtained from experimental measurements. Good agreement demonstrates the accuracy of the proposed model.

Keywords and phrases: stainless steel, turning, FEM, temperature of stainless steel, chamfered main cutting edge.

Received October 30, 2009

1. Introduction

In metal cutting, at least one fifth of all applications are turning operations. The cutting efficiency increases significantly, if the machine tool and the cutting tool are suitably selected. Suitable tools need sufficient hardness and should be of appropriate geometry. Besides the cutting velocity and cutting depth, the rate of feed plays an important role in an efficient cutting operation. As for the other cutting variables, an optimal choice of side rake angle (α_s), and of the nose radius of the tool influences the cutting quality. In general, stainless steels have high viscosity, poor heat conductivity, and are apt to cohere to a tool during cutting, thus it is difficult to cut them (Divine JR [6]). Nearly, all the work applied in the process of metal cutting is converted into heat as friction is overcome, and cutting temperature is an important parameter in the analysis of metal cutting. The heat is dissipated by the four components involved in processing the material: the cutting tool, the workpiece, the chip formed, and the cutting fluid. Most of the heat generated comes from chip formation, with most of this heat passed into the chip, while some of the heat is conducted into the workpiece. Turning is essential for stainless steel machining, particularly for austenitic stainless steel, which leads to the formation of built-up edges during cutting. However, it is difficult to machine stainless steel. The cutting tools wear rapidly because of high cutting temperature, and strong adhesion at the tool-chip interface and tool-workpiece material interface (Trent [19]). Analysis of the thermal fields in metal cutting has been a topic of research interest for many years. Obviously, it is necessary and significant to establish the nature and distribution of the metal-cutting temperatures. Many experimental techniques for measuring the metal-cutting temperatures can also be found in the literature (Boothroyd [2], Leshock and Shin [12], Amdt and Brown [1], Kato et al. [9], Wright [24]). The drawbacks of the many simplified assumptions associated with the analytical solutions were overcome by the finite element analysis (FEA) of Tay et al. [18]. FEA considers the variations in velocity, strain, and strain rate of different deformation zones, treating the tool chip and workpiece combination as a single continuum.

Finite element model (FEM) simulation is found to be useful for studying the cutting process and chip formation. FEMs are widely used for calculating the stress, strain, strain rate, and temperature distributions in the primary, secondary, and tertiary sub-cutting zones. A FEM combined with inverse method of thermoelastic-plastic material under large deformation for oblique cutting is presented. Singamneni [17] demonstrated that the mixed finite and boundary element model that can estimate cutting temperatures is simple, efficient, and at the same time, easy to implement. The temperature distribution is consistent with previous conclusions, with the peak temperature on the rake face at some distance from the cutting edge, and it also conforms to the crater wear phenomenon. Fuh and Chang [8] and Chang [5] presented a FEM model that correlate closely with the experimental values, and predict values of the cutting force and cutting temperatures in turning stainless steel with a sharp chamfered cutting edge tool. Analysis of the three-dimensional cutting temperature with a nose radius tool has received extensive attention. However, the cutting temperatures of nose radius tools were excluded from the discussion. The aim of this paper is to clarify the temperatures of stainless steel with the chamfered main cutting edge nose radius tools.

2. Theoretical Analysis

The FEM was first applied in the 1970s, greatly improving the accuracy of simulations (Fang and Zeng [7]). Klamecki [10] first introduced the application of FEM in the field of machining. Lajczok [11] developed a simplified orthogonal cutting model from the chip geometry and tool forces obtained from his experiment, while neglecting the presence of chips. Usui and Shirakashi [23] first assumed the shear cutting angle, chip geometry, and flow lines in order to predict factors such as stress, strain, and temperature. Shamoto and Altintas [15] demonstrated that the mechanics of oblique cutting are defined by five expressions. Three of the expressions are obtained from the geometry of oblique cutting, and the remaining two are derived by applying either maximum shear stress or minimum energy principle. Since temperature is of fundamental importance in metal cutting operations, many attempts

have been made to predict it. Some works simply use the relationship between the work done, and the volume of metal involved in the process to obtain an average temperature. Others use computers to derive the temperature distribution. However, the methods for measuring temperature in metal cutting have not been improved much, so it is difficult to prove the theoretical results in a precise manner.

The energy shear plane conversion in metal cutting takes place mainly in three regions, the primary deformation zone and the secondary deformation zone, a third heat source develops in most practical cases at the wear land on the flank of the tool. It is also always safe to assume, as a first approximation, that all of the work done during the deformation process gets converted into heat (Shaw [16]). Most of the heat generated at the shear plane goes into the chip and leaves the problem zone. A portion of this heat enters the workpiece. The main part of the heat generated has little influence on the performance of the tool, since the chip leaves the contact area very quickly. Usui and Hirota [20], [22], and Usui et al. [21] used an iterative technique to find the chip flow direction that minimized the sum of shear and friction energies. They did so by calculating the shear energy of a series of parallel effective shear planes (consisting of the cutting velocity and chip flow vector) along the active cutting edge. Chang [5] presented a model for sharp tools with a chamfered main cutting edge that can predict the cutting temperatures. A three-dimensional cutting model with a nose radius tool is a simple case including main and front cutting edges, as shown in Figures 1, 2, and 3. Prediction of the cutting temperatures and forces with chamfered main cutting edge nose radius tools depends on nose radius R , cutting depth d , feed rate f , cutting speed V , first-side rake angle α_{s1} , second-side rake angle α_{s2} , parallel back rake angle α_b , side cutting edge angle C_s , and the end cutting edge angle C_e . The process for deriving the shear plane A and friction plane Q are divided into segments with tool nose radius, rate of feed, and depth of cut as shown in Figure 3. The areas of the shear plane A and the projected area Q of the various cases are obtained as follows.

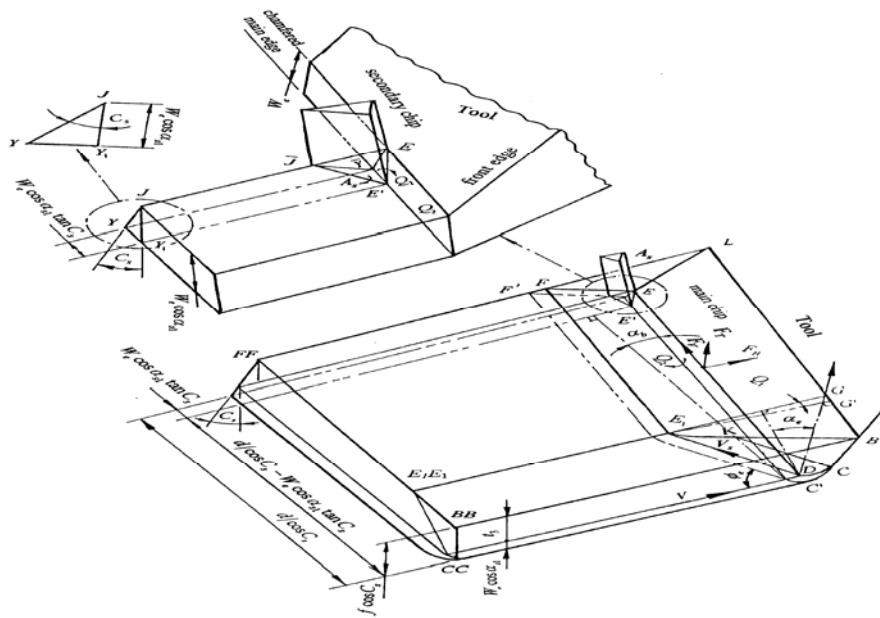
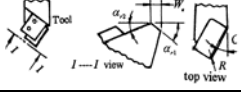


Figure 1. Basic model of the chamfered main cutting edge tool, $f < R$, $R \neq 0$.

Table 1. Tool geometry specifications (chamfered main cutting edge)

Side cutting edge angle C_s	No. of tools	Side rake angles, $\alpha_{s1}, \alpha_{s2}(\alpha_{r1}, \alpha_{r2})$	Nose roundness (R)
20°	1	10°, -10° (10°, -10°)	0.1, 0.3, 0.5, and 0.8(mm)
20°	2	20°, -20° (20°, -20°)	0.1, 0.3, 0.5, and 0.8(mm)
20°	3	30°, -30° (30°, -30°)	0.1, 0.3, 0.5, and 0.8(mm)
30°	4	10°, -10° (10°, -10°)	0.1, 0.3, 0.5, and 0.8(mm)
30°	5	20°, -20° (20°, -20°)	0.1, 0.3, 0.5, and 0.8(mm)
30°	6	30°, -30° (30°, -30°)	0.1, 0.3, 0.5, and 0.8(mm)
40°	7	10°, -10° (10°, -10°)	0.1, 0.3, 0.5, and 0.8(mm)
40°	8	20°, -20° (20°, -20°)	0.1, 0.3, 0.5, and 0.8(mm)
40°	9	30°, -30° (30°, -30°)	0.1, 0.3, 0.5, and 0.8(mm)
Notation: tool holder and tips			Carbide tips (Sandvik P10)

2.1. Shear areas of the cutting process with a chamfered main cutting edge nose radius tools

(1) The nose radius of the tool (R) is smaller than the rate of feed (f), $R < (f \cos C_s) / (1 + \sin(C_s - C_e))$ (Figure 1). The shear plane A includes both the area of A_1, A_3, A_s , and the cylindrical area A_2 , formed by the tool nose radius (Fuh and Chang [8]).

$$A = A_1 + A_2 + A_3 + A_s, \quad (1)$$

$$A_1 = 0.25 \times [4a^2n^2 - (a^2 + n^2 - c^2)^2]^{1/2}, \quad (2)$$

$$A_2 = (1 / \cos \eta_c) \int_0^{\frac{\pi}{2} + C_e - C_s} (f_1 \cos C_s - R + R \cos \Phi) d_s, \quad (3)$$

$$A_3 = f_1 \cos C_s [2(d - R + R \sin C_s) / \cos C_s f_1 (\cos C_s \tan \eta_c' + \sin C_s)] \\ \{(\cos^2 \alpha_{s2} - \sin^2 \phi_e) [\tan \eta_c \cos \eta_c' - \cos \alpha_{s2} \sin \alpha_b \\ (\cot \phi_e + \tan \alpha_e)^2]^{1/2} / (2 \cos \eta_c' \sin \phi_e \cos \alpha_{s2} \cos \alpha_b)\}, \quad (4)$$

$$A_s = 0.5(W_e \cos \alpha_{s1})^2 \tan C_s. \quad (5)$$

The friction area of the cutting cross section Q is equal to $Q_1 + Q_2 + Q_3$.

$$\begin{aligned} Q_1 = & \{f_1[d - 0.5 \cdot f_1 \sin C_s \cos C_s - R(1 - \sin C_s - \cos C_s)] \\ & - R^2[1 - \pi/4 + \tan(C_e - C_s)/2 - 0.5(C_e - C_s)] - 0.5\{f_1 \cos C_s \\ & - R[1 + \tan[(C_e - C_s)/2]]\}^2 \cdot [\tan(C_e - C_s)/(\cos \alpha_{s2} \cos \alpha_b)\}, \quad (6) \end{aligned}$$

$$Q_2 = W_e \cos \alpha_{s1} [(d / \cos C_s - W_e \cos \alpha_{s1} \tan C_s) / \cos \alpha_b], \quad (7)$$

$$Q_3 = 0.5[(W_e^2 \cos^2 \alpha_{s1} \cdot \tan C_s) / \cos \alpha_b] \quad (Q_3 \text{ is the area of triangle } DD'\bar{Y}). \quad (8)$$

Expressions for f_1 , a , n , c , e , g , η_c' , d_s , and Φ are shown in Appendix A; the angles Φ and η_c' are defined in Figure 1.

(2) The nose radius of the tool (R) is larger than the feed rate (f), $R \geq (f \cos C_s)/(1 + \sin(C_s - C_e))$ (Figure 2). Accordingly, the depth of cut (d) can be subdivided into three parts as, (a) $d > R$, (b) $d = R$, and (c) $d < R$ (Figures 3a, 3b, 3c) (Fuh and Chang [8]).

(i) $d > R$,

$$A = A_1 + A_2 + A_3 + A_s = \int_{\Phi_2}^{\Phi_1} f_I(\Phi) d_s + \int_{\Phi_0}^{\Phi_2} f_{II}(\Phi) d_s + A_3 + A_s, \quad (\text{Figure 3a}) \quad (9)$$

$$\begin{aligned} A_3 = & 0.5f_1\{2[d - R(1 - \sin C_s)] - f_1 \cos^2 C_s \tan \eta_c' - f_1 \sin C_s \cos C_s\} \\ & \{ \cos^2 \alpha_e - \sin^2 \phi_e [e - \sin^2 \phi_e \sin \eta_c - (\sin \alpha_e + \cos \alpha_e \cot \phi_e) \\ & \sin \alpha_b]^2 \}^{1/2} / (\cos \eta_c' \sin \phi_e \cos \alpha_e \cos \alpha_b), \quad (10) \end{aligned}$$

$$A_s = 0.5(W_e \cos \alpha_{s1})^2 \tan C_s. \quad (5)$$

When $d \geq R(1 - \sin C_s)$, $Q = Q_1 + Q_2 + Q_3$.

$$Q_1 = \{R^2 \tan^{-1}[(0.5f_1 / (R^2 - (0.5f_1)^2)]^{1/2} + 0.25f_1(4R^2 - f_1^2)^{1/2} + f_1(d - R)\} / (\cos \alpha_{s2} \cos \alpha_b), \quad (11)$$

$$Q_2 = W_e \cos \alpha_{s1} [(d / \cos C_s - W_e \cos \alpha_{s1} \tan C_s) / \cos \alpha_b], \quad (7)$$

$$Q_3 = 0.5[(W_e^2 \cos^2 \alpha_{s1} \cdot \tan C_s) / \cos \alpha_b] \quad (Q_3 \text{ is the area of triangle } DD' \bar{Y}). \quad (8)$$

(ii) $d = R$,

$$A = A_1 + A_2 + A_3 + A_4 + A_s = \int_{\Phi_2}^{\Phi_1} f_I(\Phi) d_s + \int_{\Phi_3}^{\Phi_2} f_{II}(\Phi) d_s + \int_{\Phi_0}^{\Phi_3} f_{III}(\Phi) d_s + A_4 + A_s, \quad (\text{Figure 3b}) \quad (12)$$

$$A_4 = \{0.5(d - R + R \sin C_s)^2 / [\sin \phi_e \cos \alpha_e \sin(\eta_e + C_s)] \{[\cos^2 \alpha_e - \sin^2 \phi_e] [\sin \eta_e - (\sin \alpha_e + \cos \alpha_e \cot \phi_e) \sin \alpha_b]^2\}^{1/2} / (\cos \alpha_b \cos C_s), \quad (13)$$

$$A_s = 0.5(W_e \cos \alpha_{s1})^2 \tan C_s. \quad (5)$$

Functions of $f_I(\Phi)$, $f_{II}(\Phi)$, and $f_{III}(\Phi)$ and the variables Φ_1 , Φ_2 , and Φ_3 are given in Appendix B.

(iii) $d < R$,

$$A = A_1 + A_2 + A_s = \int_{\Phi_2}^{\Phi_1} f_I(\Phi) d_s + \int_{\Phi_0}^{\Phi_2} f_{II}(\Phi) d_s + A_3, \quad (\text{Figure 3c}) \quad (14)$$

$$A_s = 0.5(W_e \cos \alpha_{s1})^2 \tan C_s. \quad (5)$$

$$Q = Q_1 + Q_2 + Q_3,$$

$$Q_1 = \{[R^2 \tan^{-1} f_1 / (4R^2 - f_1^2)]^{1/2} + 0.25f_1(4R^2 - f_1^2)^{1/2}$$

$$\begin{aligned}
 &+ 0.25(d - R)f_1 + \sqrt{d(2R - d)} - [f_1^2 - d^2 \\
 &+ 2R[d - f_1 \sin(\tan^{-1} \sqrt{d(2R - d)}) / (R - d)]^{1/2}], \quad (15)
 \end{aligned}$$

$$Q_2 = W_e \cos \alpha_{s1} [(d / \cos C_s - W_e \cos \alpha_{s1} \tan C_s) / \cos \alpha_b], \quad (7)$$

$$Q_3 = 0.5[(W_e^2 \cos^2 \alpha_{s1} \cdot \tan C_s) / \cos \alpha_b] \quad (Q_3 \text{ is the area of triangle } DD' \bar{Y}). \quad (8)$$

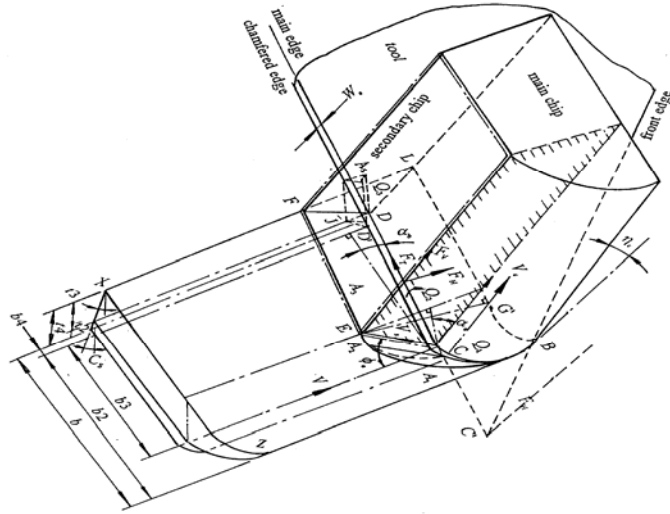


Figure 3(a). $d > R$.

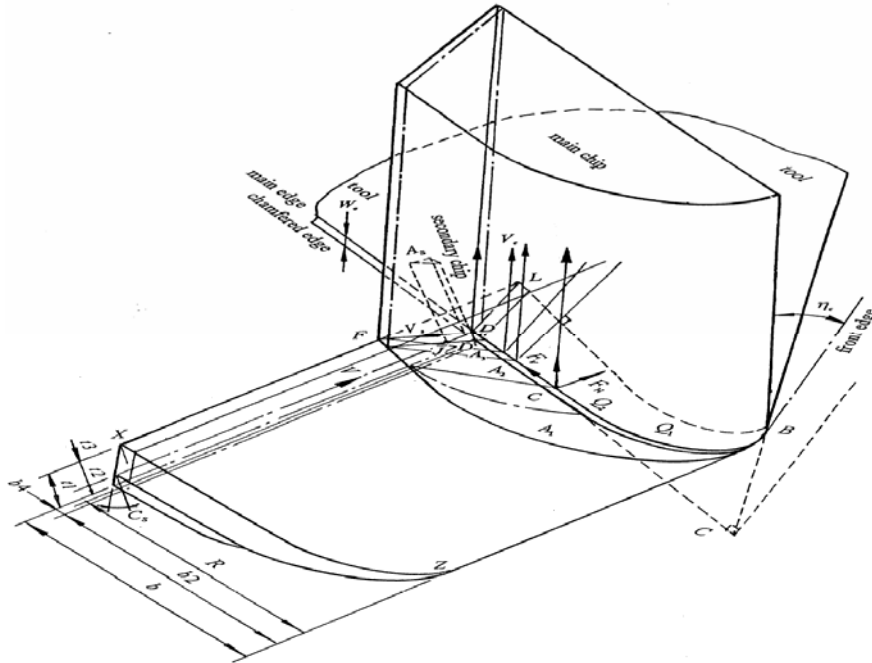


Figure 3(b). $d = R$.

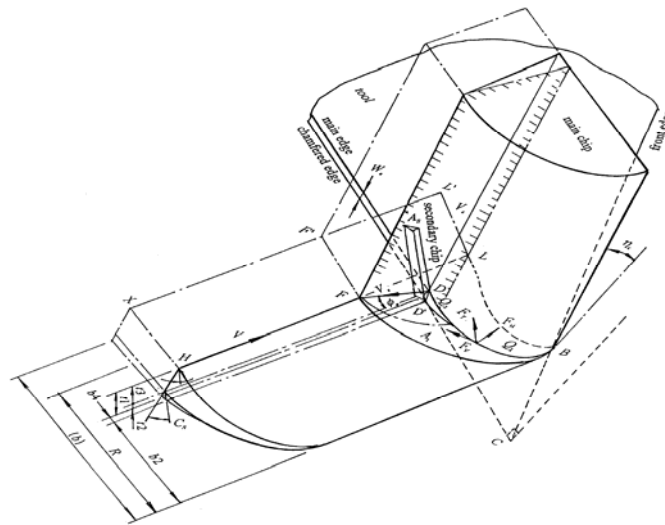


Figure 3(c). $d < R$.

Figure 3. Basic model of the chamfered main cutting tool nose radius tools, (a) $d > R$, (b) $d = R$, and (c) $d < R$ ($f > R$, $R \neq 0$).

2.2. Energy method to predict the friction cutting force

In this paper, we notice that (1) $R < (f \cos C_s)/(1 + \sin(C_s - C_e))$, (2) $R \geq (f \cos C_s)/(1 + \sin(C_s - C_e))$ will be studied in future.

The shear energy per unit time U_s , and the friction energy per unit U_f can be determined by the following equations.

That is,

$$U_s = F_s V_s = \tau_s A \cos \alpha_e V / \cos(\phi_e - \alpha_e), \quad (16)$$

$$U_f = F_c V_c = \tau_s \sin \beta \cos \alpha_e Q V / [\cos(\phi_e + \beta - \alpha_e) \cos(\phi_e - \alpha_e)], \quad (17)$$

in which

$$F_s = \tau_s A, \quad V_s = V \cos \alpha_e / \cos(\phi_e - \alpha_e),$$

$$V_c = V \sin \phi_e / \cos(\phi_e - \alpha_e),$$

represented by

$$U = U_s + U_f. \quad (18)$$

The values of A are calculated according to Equations (1)-(5), and the values of Q are calculated from Equations (6)-(8). The experimental values of α_e , β , ϕ_e , and τ_s are obtained as follows: α_e represents the effective rake angle, that is, $\alpha_e = \sin^{-1}(\sin \alpha_n \cos i + \sin \eta_c \sin i)$, β is the friction angle, which equals to $\exp(0.848\alpha_e - 0.416)$, ϕ_e is the effective shear angle and equals to $(0.581\alpha_e - 1.139)$ proposed by Usui et al. [21], τ_s is the shear stress, which equals to $571 - 19.9\alpha_e \text{ MN/m}^2$ (stainless steel) (Chang [4]), and η_c is the chip flow angle, which can be determined by considering minimum the energy U_{\min} and according to the computer flow chart (Figure 4). All the angles are expressed in radians for digital computation. In the following, the cutting force F_H can be determined by applying the proposed equation $VF_H = U_s + U_f = U$ for U_{\min} in conjunction with the energy method (R. E. M. method) (Ravindran et al. [14]), and V is the cutting speed. Therefore,

$$(F_H)_{U_{\min}} = U_{\min} / V = \{ \tau_s \cos \alpha_e \cdot A / \cos(\phi_e - \alpha_e) + \tau_s \sin \beta \cos \alpha_e \\ Q / [\cos(\phi_e - \alpha_e + \beta) \cos(\phi_e - \alpha_e)] \}. \quad (19)$$

To obtain the value of $(F_H)_{U_{\min}}$ from Equation (19), $(F_H)_{U_{\min}}$ is equated to the principal component of resultant cutting force R_t , which consists of F_t and N_t .

$$(R_t)_H = N_t \cos \alpha_{s2} \cos \alpha_b + (F_t)_{U_{\min}} \sin \alpha_e = (F_H)_{U_{\min}}, \quad (20)$$

where the frictional force is determined by

$$F_t = \tau_s \sin \beta \cos \alpha_e Q / [\cos(\phi_e + \beta - \alpha_e) \sin \phi_e]. \quad (21)$$

Therefore, N_t is rewritten as

$$N_t = [(F_H) - (F_t)_{U_{\min}} \sin \alpha_e] / (\cos \alpha_{s2} \cos \alpha_b). \quad (22)$$

The values of F_T and F_V are determined from the components of N_t and F_t . That is,

$$F_T = -N_t \cos \alpha_{s2} \sin \alpha_b + F_t (\sin \eta_c \cos \alpha_b - \cos \eta_c \sin \alpha_{s2} \sin \alpha_b), \quad (23)$$

$$F_V = -N_t \sin \alpha_{s2} + F_t (\cos \eta_c \cos \alpha_{s2}), \quad (24)$$

where N_t , the normal force on the tip is a surface with minimum energy; and $(R_t)_H$ is the horizontal cutting force in the horizontal plane.

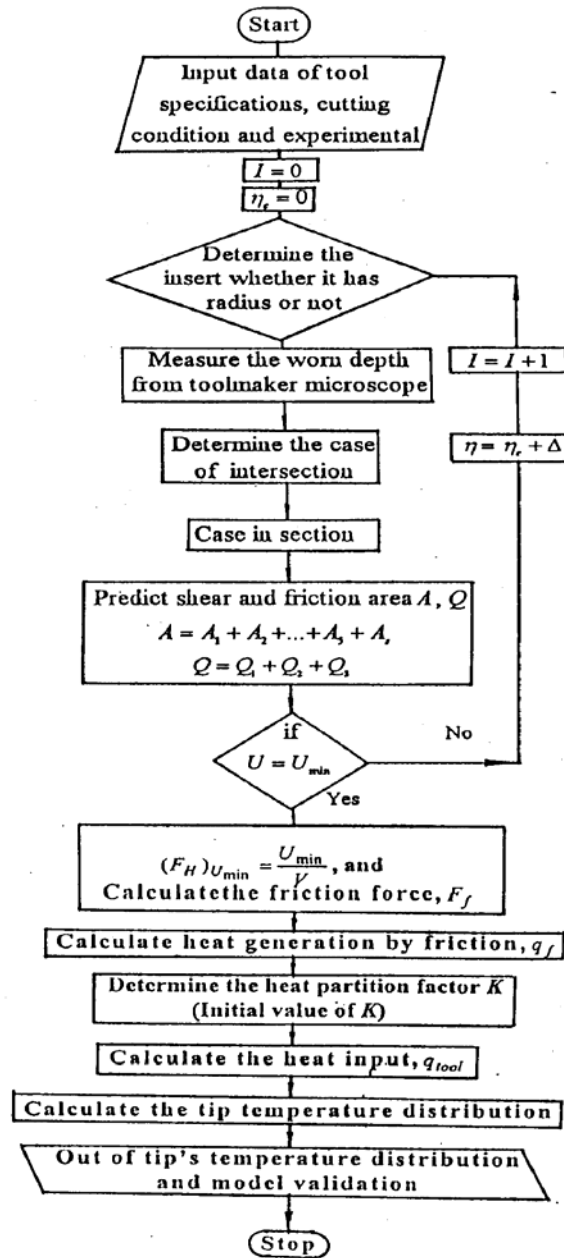


Figure 4. Flow chart of the friction force and inverse heat transfer solution.

2.3. Solid modelling of carbide tip

The chamfered main cutting edge tool has a more complex geometry. To develop a 3D FEM for thermal analysis, a solid model of the tip can be established in three steps. First, the tip cross-section profile (TCSP) perpendicular to the main cutting edge was measured by using a microscope, then CAD software, Solid Works™, was employed to generate the tip body by sweeping the TCSP, along the main cutting edge with the specified pitch. Finally, the tip's main cutting edge was simulated to remove unwanted material, and create a solid model of turning tip geometry, as shown in Figure 5.

2.4. Finite element model

The finite element analysis software Abaqus™ is used in this study. The finite element mesh of the carbide tip is shown in Figure 5, which was modelled by 58,000 four-node hexahedral elements. As shown in the top view of Figure 5, 8*6 nodes are located on the projected contact length between the tool and the workpiece, 3*6 nodes are located on the chamfered width of the main cutting edge, and 1*6 nodes are placed on the flank wear. These should provide a reasonable solution in the analysis of tip temperature distribution in turning. The initial condition of FEA has a uniform temperature of 25°C in the tip. Because, the tip does not rotate in the experiment, free convection boundary condition is used, when applied to the surface of tip contact with the workpiece.

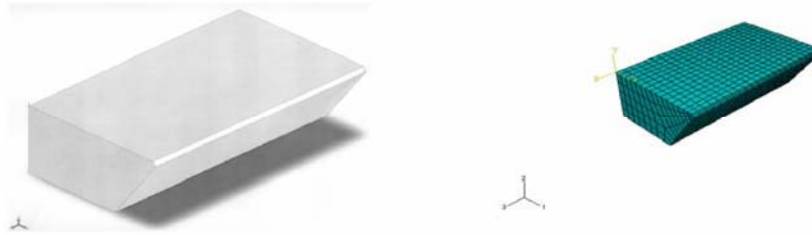


Figure 5. Solid model of the chamfered main cutting edge tool.

2.5. Modified carbide tip temperature model

Magnitude of the tip's load is shown in the following Equations (25) and (26).

$$K = U_f / A', \quad (25)$$

$$A' = L_p(d + W_e + V_b), \quad (26)$$

where A' is the area of friction force action, U_f is the friction energy, W_e is the tip's chamfered width, d is the cutting depth, V_b is the flank wear of the tip, and for simplification, the value of V_b is set to be 0.1mm. L_f is the contact length between the cutting edge and the workpiece, as in Equations (27), (29), and (31), L_p is the projected contact length between the tool and the workpiece, as referred to in Figure 6, and can be determined by Equations (28), (30), and (32), as the following conditions.

$$(1) R < (f \cos C_s) / (1 + \sin(C_s - C_e)), \quad (\text{Figure 1})$$

$$\begin{aligned} L_f &= Ph + hj + (jok + dg) / \cos \alpha_{s2} \\ &= (d - R) / \cos C_s + R(\pi / 2 - C_s + C_e) / \cos \alpha_{s2} \\ &\quad + f_1 \cos C_s / [\cos(C_e - C_s) \cos \alpha_{s2}] - R \cdot \tan C_e / \cos \alpha_{s2}, \end{aligned} \quad (27)$$

$$\begin{aligned} L_p &= [(d - R) / \cos C_s + R \tan C_s] \sin C_s + 0.5R(\pi / 2 - C_s + C_e) \sec \alpha_{s2} \\ &\quad \times \cos(\pi / 2 - C_s) + \{f_1 \cos C_s / [\cos(C_e - C_s) \cos \alpha_{s2}] \\ &\quad - R \tan C_s / \cos \alpha_{s2}\} \cos C_e. \end{aligned} \quad (28)$$

$$(2) R \geq (f \cos C_s) / (1 + \sin(C_s - C_e)), \quad (\text{Figures 2 and 3})$$

$$(i) \text{ when } d \geq R(1 - \sin C_s), \text{ then}$$

$$\begin{aligned} L_f &= ph + hj + jok / \cos \alpha_{s2} \\ &= (d - R) / \cos C_s + R \tan C_s + R[0.5\pi - C_s + \sin^{-1}(f_1 / 2R)] / \cos \alpha_{s2}, \end{aligned} \quad (29)$$

$$L_p = [(d - R) / \cos C_s + R \tan C_s] \sin C_s + R(0.5\pi - C_s)$$

$$\times \cos[(0.5\pi - C_s)/2 + \sec \alpha_{s2} R \sin^{-1} f_1 / 2R \cos[\sin^{-1}(f_1 / 2R)/2]]. \quad (30)$$

(ii) $d < R(1 - \sin C_s)$, then

$$L_f = R(\theta_1 + \theta_2) = R[\sin^{-1}(f_1 / 2R)][\cos^{-1}(R - d) / R], \quad (31)$$

$$L_P = R \sin^{-1}(f_1 / 2R) \cos[\sin^{-1}(f_1 / 2R)] / 2 + R \cos^{-1}((R - d) / R) \cos[\sin^{-1}(R - d) / 2] / 2. \quad (32)$$

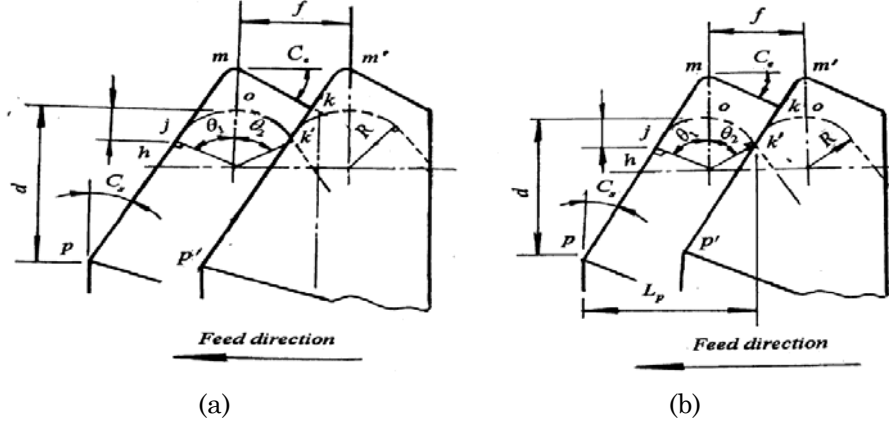


Figure 6. Calculation of contact length (a) L_f , (b) L_P between cutting tool and workpiece at $f > R$, $R \neq 0$.

$$\rho c \frac{\partial T}{\partial t} = k \frac{\partial^2 T}{\partial x^2} + k \frac{\partial^2 T}{\partial y^2} + k \frac{\partial^2 T}{\partial z^2}, \quad (33)$$

where ρ is the density, c is the thermal conductivity, and k is the heat capacity.

The boundary condition on the square surface at the cutting edge, opposite from the turning tip, also assumed to be maintained in turning, is assigned to be 25°C. The heat generated in turning is applied as a line load on the main cutting edge. The contact between tool and chip is wide in stainless steel machining according to Equations (27) and (28). Compared with the 0.36mm feed per revolution, the characteristic length of the elements at tip and cutting edges is much larger, around 3.29mm.

This allows the use of line heat flux at the cutting edge in FEA. In heat generation, the cutting edge is assumed to be perfectly sharp; the friction force is multiplied by the chip velocity to give the line heat generation rate, q_f on cutting edge.

$$q_f = F_f V_c. \quad (34)$$

Assuming that, K is the heat partition factor for determining the ratio of heat transferred to the tool, the heat generation rate, q_{tool} on each cutting edge is:

$$q_{tool} = Kq_f. \text{ (Li and Shih [13])} \quad (35)$$

In this study, K is assumed to be a constant for all cutting edges. The inverse heat transfer method is employed to find the value of K , under certain turning speeds.

2.6. Inverse heat transfer solution and validation

The flowchart for inverse heat transfer solution of K was obtained by the Abaqus™ solver and is summarized in Figure 4. By assuming a value for K , the spatial and temporal temperature distribution of the tip can be found. The inverse heat transfer method is employed to solve K by minimizing an energy function on the tip surface is determined by Equations (34) and (35), as shown in Figure 5. Using an estimated value of K , the heat generation rate is calculated and applied to nodes on the tip's main and end cutting edges. The discrepancy between the experimentally measured temperatures by infrared pyrometer j by time t_i , $T_j^{t_i}|_{\text{exp}}$ is

$$Obj(K) = \sum_{i=1}^{n_i} \sum_{j=1}^{n_j} (T_j^{t_i}|_{\text{exp}} - T_j^{t_i}|_{\text{est}})^2, \text{ (Li and Shih [13])} \quad (36)$$

where n_i is the number of time instants during turning, and n_j is the number of thermocouples selected to estimate the objective function.

After finding the value of K , the FEM can be employed to calculate the temperature at locations of thermocouples not used for inverse heat transfer analysis. The tool tip's temperature predicted from the FEA is compared with experimental measurements to validate the accuracy of the proposed method.

3. Experimental Procedures

The experimental set-up is shown in Figure 7. The machine tool used for the test is the *Victor*, 600*700 lathe. In Figure 7, the workpiece is held in the chuck of the lathe, and the cutter is mounted on a dynamometer (Kistler type 9257B) to measure the three-axis component forces. The force signals are recorded through charge amplifiers and *A / D* converter. An infrared detector is utilized to monitor the cutting tips, and the temperature acquired is stored in the computer. All the measured data are recorded by a data acquisition system (Keithley Metrobyte Das-1600), and analyzed by the control software (Easyest). The workpieces are stainless steel, SUS 304 of 65mm in diameter; and 500mm lengths cut from the same bar are used. The composition of workpiece is C = 0.05%, Mn = 1.17%, P = 0.34%, S = 0.24%, Si = 0.29%, Ni = 9.14%, Cr = 18.45%, 168HB. The cutting tools used in the experiments are Sandvik p10, type S1P (Brookes [3]). Carbide-tipped tools with following angles are used: back rake angle = 0° , side rake angle = 6° , end relief angle = 7° , side relief angle = 9° , end cutting edge angle = 70° , side cutting angles = 20° , 30° , and 40° , and nose radius = 0.1~0.3mm. Tool characteristics include WC 69%, TiC 15%, TaC 8%, Co 8%, HV = 1740, density = 10.3g/cm^3 , thermal conductivity = $25\text{W/m}^\circ\text{K}$, and heat capacity = $210\text{J/Kg}^\circ\text{K}$. The tool geometries are summarized in Table 1. The experimental tests were conducted under the following conditions: dry cutting; cutting velocity 40-148m/min; cutting depth 1 and 2mm; feed rate 0.33mm/rev; the tool holder being vertical to the workpiece; and protrusion of tool tip from the dynamometer being 30mm. For each tool configuration, the workpiece is turned to be a length of 240mm in the feed direction. The data are recorded three times at different sections, and average values are taken. The shapes of the main and the secondary tips are observed. Block diagrams of performance are drawn, as shown in Figure 4.

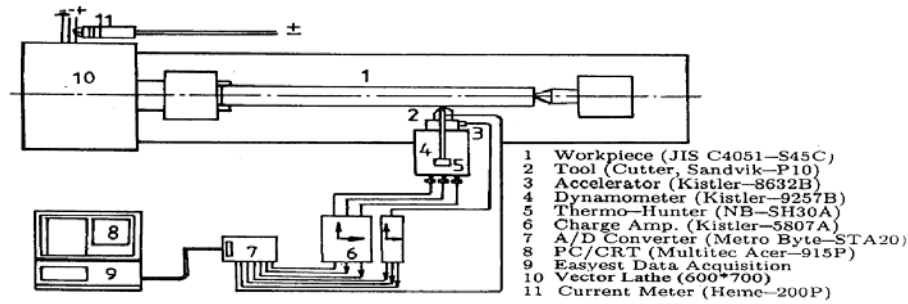


Figure 7. Experimental set-up.

4. Results and Discussion

The temperature measured by infrared on the tip surface is used as input for the inverse heat transfer method to predict the heat flux on the chamfered main cutting edge nose radius tools. This method determines the heat partition factor by using the optimization method. An infrared (IR) pyrometer system is developed to measure the temperature during turning with a nose radius chamfered main cutting edge tool. For knowing the temperature of cutting tools, and how this chamfered main cutting edge nose radius tools decreases the temperature of the tool tip surface, is indicated in the following. As mentioned by Li and Shih [13], according to Equations (35) and (36), the flowchart for inverse heat transfer solution of K is described in Figure 4. The results obtained from the finite element analyses are shown in Figures 8-11, and described as follows:

(1) Figure 8 shows the cutting temperatures vs. cutting time for different values α_{s1} , α_{s2} , and C_s with chamfered nose radius tool at $d = 2.0\text{mm}$, $f = 0.33\text{mm/rev}$, $V = 120\text{m/min}$, and $R = 0.1\text{mm}$. Figure 9 shows the cutting temperatures vs. C_s , for different values R with chamfered nose radius tool at $\alpha_{s1} = -30^\circ$, $\alpha_{s2} = 30^\circ$, $d = 2.0\text{mm}$, $f = 0.33\text{mm/rev}$, $V = 120\text{m/min}$, respectively. Figure 10 shows the cutting temperatures vs. R for different values α_{s1} , α_{s2} , and C_s with chamfered nose radius tool, at $d = 2.0\text{mm}$, $f = 0.33\text{mm/rev}$, and

$V = 120\text{m/min}$. Figure 11 shows the cutting temperature of chamfered cutting edge nose radius insert at $C_s = 30^\circ$, $R = 0.3\text{mm}$, $\alpha_{s1} = -30^\circ$, and $\alpha_{s2} = 30^\circ$, $d = 2.0\text{mm}$, $f = 0.33\text{mm/rev}$, and $V = 120\text{m/min}$.

(2) For a constant nose radius R , Figures 8 and 9 show that increasing the side rake angles, α_{s1} , α_{s2} , and C_s , reduces the cutting temperature. The reason is that, the contact length between the chip and the tool is shortened, thus, causing the effective rake angle, effective shear angle to increase and the friction force to decrease.

(3) As seen in Figures 8 and 9, the cutting-edge temperature of the chamfered main edge nose radius tool at $C_s = 30^\circ$, $\alpha_{s1} = -30^\circ$, and $\alpha_{s2} = 30^\circ$ the lowest, while the highest is $C_s = 20^\circ$, $\alpha_{s1} = -10^\circ$, and $\alpha_{s2} = 10^\circ$, and the temperature does not exceed 400°C .

(4) From Figures 9 and 10, for $C_s = 30^\circ$, $\alpha_{s1} = -30^\circ$, $\alpha_{s2} = 30^\circ$, and $R = 0.3\text{mm}$, it can be seen that, the cutting temperature is the lowest, because the areas of shear and friction are the smallest, but the effective rake angle and the effective shear angle are both the largest, and the inverse data correlate closely with the experimental values.

(5) From Figure 10, for constant C_s , as the nose radius (R) increased from 0.3mm to 0.8mm , the cutting temperature increased, but it decreased as R increased further from 0.1 to 0.3mm . When $R = 0.8\text{mm}$, the areas of shear and friction are the largest, and probably due to the effect of chatter leading to unstable cutting forces.

(6) Figure 11 shows that the cutting temperature of chamfered cutting edge nose radius insert is close to that seen in Figures 9 and 10.

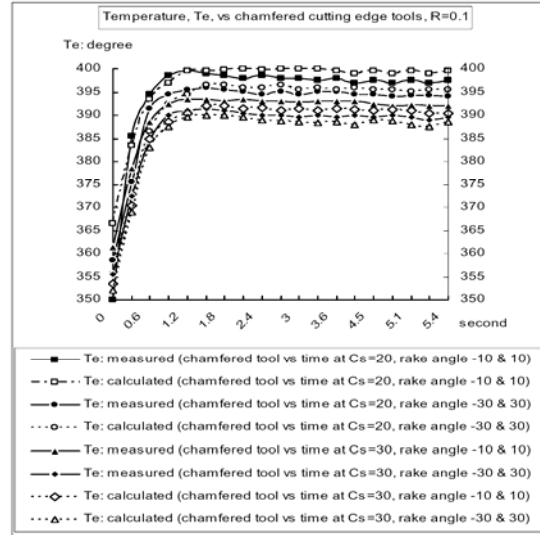


Figure 8. Cutting temperatures vs. cutting time for different values α_{s1} , α_{s2} , and C_s , with chamfered nose radius tool at $d = 2.0\text{mm}$, $f = 0.33\text{mm/rev}$, $V = 120\text{m/min}$, and $R = 0.1$, respectively (stainless steel).

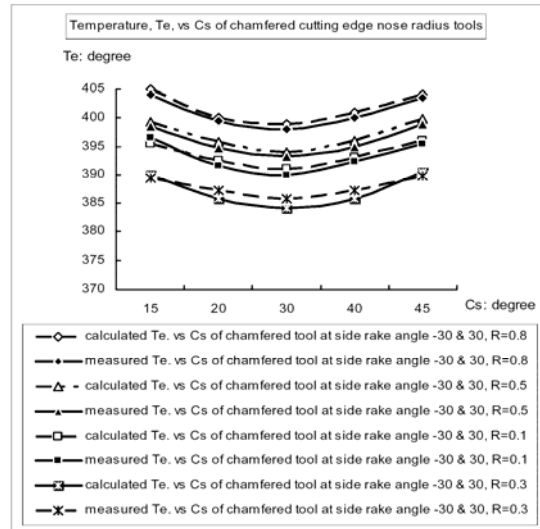


Figure 9. Cutting temperatures vs. C_s for different values R , with chamfered nose radius tool at $\alpha_{s1} = -30^\circ$, $\alpha_{s2} = 30^\circ$, $d = 2.0\text{mm}$, $f = 0.33\text{mm/rev}$, $V = 120\text{m/min}$ (stainless steel).

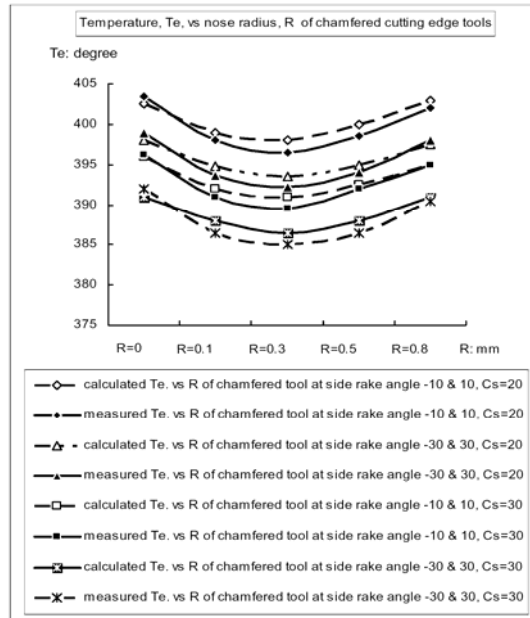


Figure 10. Cutting temperatures vs. R for different values α_{s1} , α_{s2} , and C_s , with chamfered nose radius tool at $d = 2.0\text{mm}$, $f = 0.33\text{mm/rev}$, and $V = 120\text{m / min}$, respectively (stainless steel).

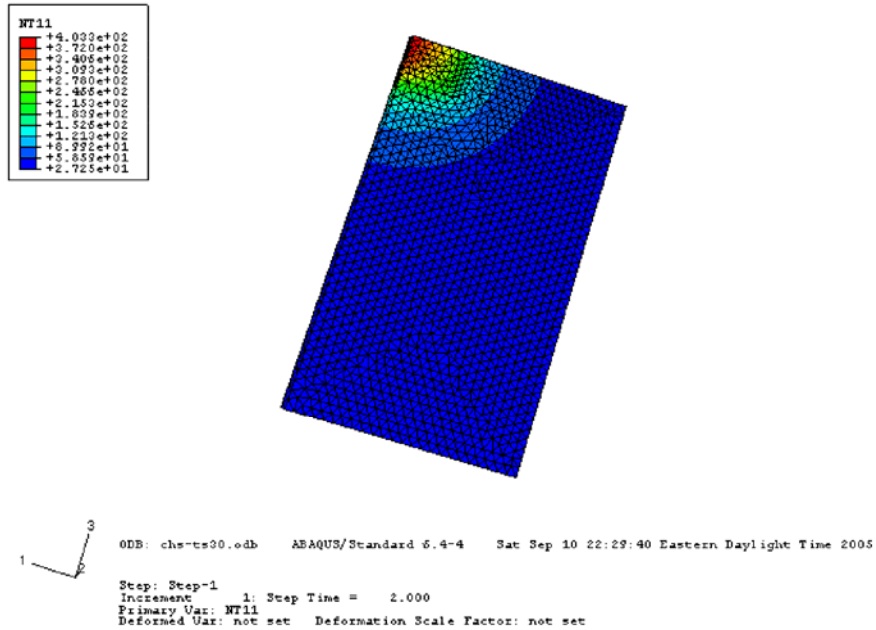


Figure 11. Temperature of chamfered cutting edge nose radius insert at $C_s = 30^\circ$, $R = 0.3\text{mm}$, $\alpha_{s1} = -30^\circ$ and $\alpha_{s2} = 30^\circ$, $d = 2.0\text{mm}$, $f = 0.33\text{mm/rev}$, and $V = 120\text{m/min}$ (stainless steel).

5. Conclusions

Good correlations were obtained between predicted values and experimental results of forces and temperatures during machining stainless steel with chamfered main cutting edge sharp tools (Chang [5]). A new model for nose radius tools with chamfered main cutting edge has been developed by including the variation in friction plane areas. In this model, the energy method is also employed for more accurate prediction of cutting force. The FEM and inverse heat transfer solution for tool temperature in stainless steel turning is obtained, and compared with experimental measurements. The good agreement demonstrates the accuracy of proposed model. This model can be extended to the on-line control domain in addition to the factors of time and thermal effect.

Additionally, this new nose radius tool model using the variation in friction areas that occur in nose radius tool can be applied to accurately predict the cutting forces and the temperature of the tool tip surface.

Acknowledgement

The work was supported by National Science Council of Taiwan (R.O.C.) under grant number NSC 2008-2212-E-197-009.

References

- [1] G. Amdt and R. H. Brown, On the temperature distribution in orthogonal machining, *Int. J. Machine Tools and Manufacture, Design, Research and Application* 119 (1966), 39-45.
- [2] G. Boothroyd, Temperature in orthogonal metal cutting, *Proc., Inst. Mechanical Engineering* 177 (1963), 7-13.
- [3] K. J. A. Brookes, *World directory and handbook of hard metals*, 5th edition, International Carbide Data Hand Book, United Kingdom, D (1992), 172-175.
- [4] C. S. Chang, Turning of stainless steel with worn tools having chamfered main cutting edges, *Int. J. Machine Tools and Manufacture, Design, Research and Application* 38 (1998), 291-313.
- [5] C. S. Chang, Prediction of the cutting temperatures of stainless steel with chamfered main cutting edge tools, *J. Mater. Process. Technol.* 190(1-3) (2007), 332-341.
- [6] C. A. Divine JR, What to consider in choosing an alloy, machining stainless steels, *American Society for Metals (ASM), U.S.A.*, (1975), 19-23.
- [7] G. Fang and P. Zeng, Three-dimensional thermoelastic-plastic coupled FEM simulations for metal oblique cutting processes, *J. Mater. Process. Technol.* 168 (2005), 42-48.
- [8] K. H. Fuh and C. S. Chang, Prediction of the cutting forces for chamfered main cutting edge tools, *Int. J. Machine Tools and Manufacture, Design, Research and Application* 35 (1995), 1559-1586.
- [9] S. Kato, Y. Yamaguchi, Y. Watanabe and Y. Hiraiwa, Measurement of temperature distribution within tool using powders of constant melting point, *ASME, J. Eng. Ind.* 98 (1976), 607-614.
- [10] B. E. Klamecki, *Incipient Chip Formation in Metal Cutting– a Three Dimensional Finite Analysis*, Ph. D. Dissertation, University of Illinois at Urbana, Champaign, 1995.

- [11] M. R. Lajczok, A Study of Some Aspects of Metal Cutting by the Finite Element Method, Ph. D. Dissertation, NC State University, 1980.
- [12] C. E. Leshock and Y. C. Shin, Investigation on cutting temperature in turning by a tool-work thermocouple technique, ASME, J. Manufacturing Science and Engineering 119 (1997), 502-510.
- [13] R. Li and A. J. Shih, Inverse Heat Transfer Solution in Tool Temperature Titanium Drilling, Mechanical Engineering, University of Michigan-Ann Arbor, 2005.
- [14] A. Ravindran, G. V. Reklaitis and K. M. Ragsdell, Region-Elimin. Method, Engineering Optimization, Methods and Applications, Wiley-Interscience, New York, U.S.A., (1984), 37-46.
- [15] E. Shamoto and Y. Altintas, Prediction of shear angle in oblique cutting with maximum shear stress and minimum energy principles, Trans., ASME, J. Manufacturing Science and Engineering 121 (1999), 399-407.
- [16] M. C. Shaw, Metal Cutting Principles, Oxford University Press, New York, (1984), 335-367.
- [17] S. B. Singamneni, A mixed solution for three-dimensional temperature distribution in turning inserts by using finite and boundary element techniques, J. Mater. Process. Technol. 166 (2005), 98-106.
- [18] A. O. Tay, M. G. Stevenson, Davis G. de Vahl and P. L. B. Oxley, A numerical method for calculating temperature distributions in machining from force and shear angle measurements, Int. J. Machine Tools and Manufacture, Design, Research and Application 16 (1976), 335-345.
- [19] E. G. Trent, Metal Cutting, Butterworth & Co. Ltd., Second Edition, England, (1984), 205-207.
- [20] E. Usui and A. Hirota, An energy approach to mechanics of three-dimensional metal cutting, Proc. Int. Conf. on Production Engineering, Japanese Society of Precision Engineering (1974), 541-546.
- [21] E. Usui, A. Hirota and M. Masuko, Analytical prediction of three-dimensional cutting process, Part 1, Basic cutting model and energy approach, Trans., ASME, J. Eng. Ind. 100 (1978), 222-228.
- [22] E. Usui and A. Hirota, Analytical prediction of three-dimensional cutting process, Part 2, Chip formation and cutting forces with conventional single-point tool, Trans., ASME, J. Eng. Ind. 100 (1978), 229-235.
- [23] E. Usui and T. Shirakashi, Mechanics of machining-from descriptive to predictive theory, on the art of cutting metals -75 years later a tribute to F. W. Taylor, ASME PED-7 (1982), 13-30.
- [24] P. K. Wright, Correlation of tempering effects with temperature distribution in steel cutting tools, ASME, J. Eng. Ind. 100 (1978), 131-140.

Appendix

A. Variables for the tool with nose radius, and where that nose radius is smaller than the feed ($R \neq 0$, $R < f$),

$$f_1 = f - W_e \cos \alpha_{s1}, \quad (\text{A1})$$

$$\alpha = \{f_1 \cdot \cos C_s - R[1 + 2 \tan(C_e - C_s) / 2]\} \\ \times \{\cos^2 \alpha_b + [\tan \alpha_{s2} \sin \alpha_b + \tan(C_s - C_e)]^2\}^{1/2} / (\cos \alpha_{s2} \cos \alpha_b), \quad (\text{A2})$$

$$n = \{f_1 \cdot \cos C_s - R[1 + \sin(C_e - C_s)] / (\cos \eta_c' \sin \phi_e)\}, \quad (\text{A3})$$

$$c = (e^2 + g^2 - 2eg \cdot \sin \alpha_b)^{1/2}, \quad (\text{A4})$$

$$e = \{f_1 \cdot \cos C_s - R[1 + 2 \tan(C_e - C_s) / 2]\} \{ \tan \eta_c \cos \alpha_b \\ - [\tan \alpha_{s2} \sin \alpha_b + \tan(C_e - C_s) \cos \alpha_{s2}] / (\cos \alpha_{s2} \cos \alpha_b), \quad (\text{A5})$$

$$g = \{f_1 \cdot \cos C_s - R[1 + \sin(C_e - C_s) \cot \phi_e \tan \alpha_e]\} / \cos \eta_c', \quad (\text{A6})$$

$$\eta_c' = \tan^{-1}[(\tan \eta_c - \sin \alpha_{s2} \tan \alpha_b) \cos \alpha_b / \cos \alpha_{s2}], \quad (\text{A7})$$

$$d_s = R / \sin \phi_e \{\cos^2(\eta_c' - \Phi) + [\cos \phi_e \sin(\eta_c' - \Phi) + / \cos \alpha_b \sin \phi_e \\ \times (\sin \alpha_b \cos \Phi - \tan \alpha_{s2} (\sin^2 \alpha_b + 1)^2 \sin \Phi)^2\}^{1/2} d\Phi, \quad (\text{A8})$$

$$\Phi = \pi / 2 + C_e + C_s. \quad (\text{A9})$$

B. Functions $f(\phi)$ and the variables Φ_1 , Φ_2 , and Φ_3 for the tool with nose radius, and where the nose radius is larger than the feed rate, ($R \neq 0$, $R > f$, $d > R$, and $d = R$).

$$f_I(\Phi) = [f_1 + R \cos(\Phi + C_s)] \{ \sin(\eta_c' + C_s) \cot [\tan^{-1}(f_1 + R \cos(\Phi + C_s)) \\ / (R \sin(\Phi + C_s))] + \cos(\eta_c' + C_s) + \cos(\eta_c' + C_s) \} \\ - R^2 \{ - (f_1 + R \cos(\Phi + C_s)) [\sin(\eta_c' + C_s) - \cos(\eta_c' + C_s) \cot$$

$$\begin{aligned} & \times [\tan^{-1}(f_1 + R \cos(\Phi + C_s)) / \cos(\eta_c' + C_s) \cot \\ & \times [\tan^{-1}(f_1 + R \cos(\Phi + C_s)) / R \sin(\Phi + C_s)]]^2 \}^{1/2}, \end{aligned} \quad (\text{B1})$$

$$\begin{aligned} f_{II}(\Phi) = & 1 / \sin(\eta_c' + C_s) \{ R \sin(\Phi + C_s) + f_1 \sin(\eta_c' + C_s) \cos C_s / \cos \eta_c' \\ & + R \sin(\eta_c' - \Phi) \cos C_s / \cos \eta_c' \} - R / \cos \eta_c', \end{aligned} \quad (\text{B2})$$

$$f_{III}(\Phi) = [d - R + R \sin(\Phi + C_s) / \sin(\eta_c' + C_s)], \quad (\text{B3})$$

$$\Phi_1 = \pi / 2 - C_s + \tan^{-1} f_1 / (4R^2 - f_1^2)^{1/2}, \quad (\text{B4})$$

$$\Phi_2 = \eta_c' - \sin^{-1} \{ (-f_1 / R) \sin(\eta_c' + C_s) + \sin \eta_c' \}, \quad (\text{B5})$$

$$\begin{aligned} \Phi_3 = & \eta_c' + \sin^{-1} \{ (1 / R) [f_1 \sin(\eta_c' + C_s) + (R \cos \eta_c' / \cos C_s) \\ & - (d \cos \eta_c' / \cos C_s) - R \sin(\eta_c' + C_s) / \cos C_s] \}. \end{aligned} \quad (\text{B6})$$

C. Function $f_{II}(\Phi)$ and variables Φ_0 and Φ_2 for the tool with nose radius, and where the nose radius is larger than the feed, ($R \neq 0$, $R > f$, $d < R$).

$$f_{II}(\Phi) = R / \sin(\eta_c' + C_s) \{ \sin(\Phi + C_s) - \sin(\Phi_2 + C_s) \} + f_I(\Phi_2), \quad (\text{C1})$$

$$\Phi_0 = -C_s + \sin^{-1} [(R - d) / R], \text{ and} \quad (\text{C2})$$

$$\Phi_2 \text{ is determined so as to satisfy the following equation.} \quad (\text{C3})$$

Nomenclatures

F_{HH} Final modified horizontal cutting force.

F_P Plowing force (N).

F_s Shear force (N).

F_t Friction force (N).

F_W Additional force due to wear (N).

L_f Length of contact between tool and work piece (mm).

L_p	Projected length of contact between tool and work piece (mm).
R	Nose radius.
σ_y	Yield normal stress (MN/mm ²).
τ_y	Yield shear stress (MN/mm ²).
τ_s	Shear stress (MN/mm ²).
R	Main cutting edge radius (mm).
T	Cutting time (min).
T_e	Temperature (°C).

